scientific reports

Check for updates

OPEN

Microsphere-Augmented PDMS integration in tapered FBG small-scale sensors for enhanced temperature sensitivity

Bryan Sanipatin[1]✉, Luis A. Sánchez[2], Lucía Arques[1] & Salvador Sales[1]

This work presents a novel high-sensitivity temperature sensor based on a fiber Bragg grating inscribed on a tapered optical fiber which terminates in a microsphere, all embedded within a PDMS-filled silica capillary. The fabricated microsphere at the taper's end enhances PDMS traction, improving strain transfer between the polymer and the fiber during temperature changes. Different waist diameters for the tapered fiber were considered for the design of the sensor. The sensor's response was analyzed over a temperature range of 20 °C to 90 °C for taper waist diameters ranging from 60 µm to 20 µm. Experimental results demonstrate a wavelength temperature sensitivity of 47.19 pm °C^{-1} for a 60 µm waist diameter and 221.2 pm °C^{-1} for a 20 µm waist diameter, achieving up to 22 times the sensitivity of a bare FBG. The experimental results were supported by finite element analysis simulations, which showed a clear correlation between the enhanced sensitivity and the increase in axial strain applied by the PDMS on the embedded fiber. This enhancement in sensitivity was demonstrated by housing the fiber in a capillary, integrating the microsphere at the end of the fiber, and diminishing the fiber taper's diameter. Moreover, unlike traditional techniques aimed at enhancing the thermal sensitivity of fiber Bragg gratings, the sensor developed through this innovative approach exhibits enhanced performance regarding both dimensions and sensitivity.

Since the discovery of fiber Bragg gratings (FBGs) in 1978 by Hill *et al.*[1], fiber Bragg grating (FBG) sensors in silica optical fibers have seen increased use in many fields, including civil engineering[2], aerospace engineering[3], the energy sector[4,5], environmental monitoring[6] or biomedical applications[7]. These sensors offer significant advantages over their electronic counterparts. Their immunity to electromagnetic interference and capability to operate in harsh environments make them a reliable option for numerous industrial applications. Their compact size and high sensitivity allow them to detect small changes in a wide range of different magnitudes[8]. The low loss of silica optical fibers in the C-band enables the monitoring of sensors over long distances with minimal signal degradation. Additionally, their ability to be wavelength-multiplexed makes it possible to install and monitor different sensors on the same fiber.

In particular, temperature sensors based on FBGs in silica optical fibers have been extensively studied due to the intrinsic sensitivity of FBGs to this magnitude. The optical wavelength reflected by the FBG depends on the grating period, which varies due to the thermal expansion of the material as the temperature changes. However, silica presents a low thermal expansion coefficient ($\sim 0.5 \times 10^{-6}{}^{\circ}\mathrm{C}^{-1}$ in the range of −100 °C to 200 °C) limiting the sensitivity of bare FBG-based sensors ($\sim 10\mathrm{pm}\ {}^{\circ}\mathrm{C}^{-1}$). To improve its sensitivity, FBGs are typically coated with different materials that increase the effective thermal response of the sensor. Metal coatings are a common approach to achieve this due to their high thermal expansion coefficient (from 10 to $30 \times 10^{-6}{}^{\circ}\mathrm{C}^{-1}$). Metals like lead[9,10], aluminum[10], zinc[11,12], copper[10–12], indium[10] or silver[12] have been successfully exploited to improve the sensitivity of FBG up to values of 3 times that of the bare FBG. However, the deposition of uniform metal coatings on optical fibers is not straightforward and requires complex processes such as chemical vapor deposition, electro-deposition and sputtering. In addition, high coating thickness is desired so that the strain in the metal is properly transferred to the fiber core, which makes layer uniformity difficult due to the cylindrical shape of the fiber.

The use of polymeric coatings has also aroused interest in recent years to achieve this purpose[13–19]. Polymer coatings are much easier to apply to the fibers using molding processes and they can present thermal

[1]Photonics Research Labs, ITEAM, Universitat Politècnica de València, Camino de Vera, S/N, 46022 Valencia, Spain. [2]CalSens S.L., Universitat Politècnica de València, 8F Building OfficeCamino de Vera S/N, 46022 Valencia, Spain. ✉email: bsanipa@upv.edu.es

expansion coefficients up to $150 \times 10^{-6\circ}C^{-1}$, 5 times higher than those of metals. Some examples of FBGs with polymeric coatings include polymethyl methacrylate[20] (PMMA), polytetrafluoroethylene[17] (PTFE), epoxy resins[18], polyimides[15,16] or acrylates[14–16,18]. Specifically, polydimethylsiloxane (PDMS) is a silicone polymer that presents a particularly high thermal expansion coefficient of $\sim 300 \times 10^{-6\circ}C^{-1}$ and it is thermally stable over a wide range of temperatures (—50 °C to 200 °C). PDMS also presents a high thermo-optic coefficient, which has been used to manufacture sensitivity-enhanced temperature sensors based on tapered fibers[21,22] and long-period gratings[23]. PDMS has also been previously used as a coating for FBGs to improve their sensitivity to temperature changes. In 2011, Chang-sub Park et al.[24] used PDMS coatings with different cross sections on FBGs, obtaining an improvement in their temperature response of up to 4 times that of a bare FBG by using a 400 mm^2 cross section coating. Due to the difference in Young's moduli of silica and PDMS, this sensitivity enhancement saturates for high cross section values, limiting its application for situations where high sensitivity and small size is required.

In this work, a new design for a high-sensitivity temperature FBG-based sensor is proposed and demonstrated. The sensor was fabricated by inscribing an FBG on a tapered optical fiber and embedding it in a PDMS-filled silica capillary. The design included a microsphere created at the end of the taper to improve the traction of the PDMS onto the fiber when expanding or contracting due to temperature changes. Finite element analysis simulations were performed to analyze the effect of including these elements in the sensor design and to obtain a comprehensive interpretation of the experimental results. The response of the sensor was studied in temperature range from 20 °C to 90 °C for different waist diameters of the taper. The experimental results showed a wavelength temperature sensitivity of the FBG ranging from 47.19 pm $°C^{-1}$ for a waist diameter of 60 µm, to 221.2 pm $°C^{-1}$ for a waist diameter of 20 µm, which yields in an improvement of up to 22 times with respect to the sensitivity of a bare FBG. A clear correlation was observed between the increased sensitivity of the sensor and the enhancement in axial strain exerted by the PDMS on the fiber by the reduction of the taper diameter, the inclusion of the silica capillary and the microsphere at the fiber-end.

Device structure

The conceptual design of the proposed device consists of three primary components: the taper-microsphere section, the fiber Bragg grating, and the PDMS-filled silica capillary. The combination of these three elements aims to take advantage of the inherent properties of the materials involved to improve the performance of this novel structure, but the same principle can be extrapolated to other combination of materials or polymers. Fig. 1 shows a two-dimensional visual clarification and an annotated drawing detailing the proposed design and its components.

Taper-microsphere section

First, for the fabrication of the taper-microsphere section, a single-mode fiber (SMF-28) is tapered using a commercial CO_2 laser splicing system (Fujikura, LZM-100) over a specified length denoted as L_S which was 4 mm in all scenarios (Fig. 2a) with a transition length L_T. Upon tapering, the fiber is cleaved (Fig. 2b) and subsequently subjected to CO_2 laser heating (Fig. 2c), a process aimed at generating a silica microsphere at the tapered fiber termination. The dimension of this sphere depends on the internal diameter of the chosen capillary; for the purposes of this study, a silica capillary with an internal diameter of 150 µm and external diameter of 365 µm was employed. To mitigate potential discrepancies between the capillary's internal diameter and the silica sphere's diameter, a margin of error akin to the capillary's tolerances (±4 µm) was implemented. In the conducted experiments, silica spheres with a diameter (D_B) of 146 microns were fabricated, ensuring compatibility with the capillary's 150-micron internal diameter (Fig. 3b). Also, the length of the transition (L_T) plays a crucial role in determining the overall size of the device, as a more extended transition will improve the optical spectral quality[25] of the device but it will be larger in size. In our study, we aimed to reduce the transition length as much as feasible to show the maximum capabilities in terms of the reduction of material involved. However, it is crucial to maintain equilibrium between the transition length and the losses incurred in the device to ensure adequate visibility of the fiber Bragg grating's spectrum.

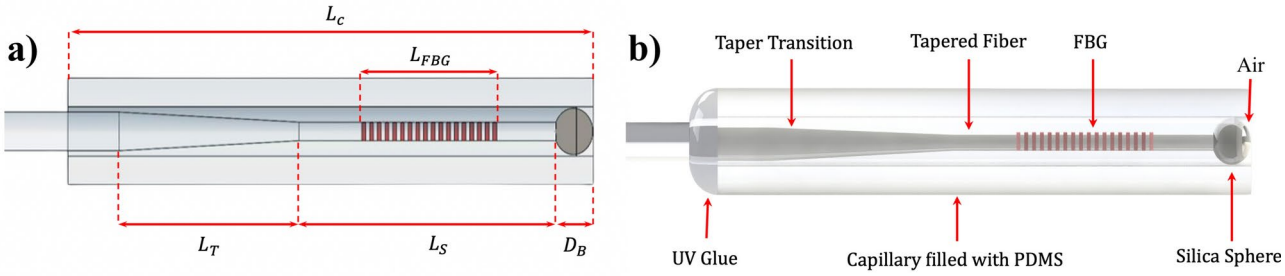

Fig. 1. (**a**) 2D Scheme of the proposed sensor. (**b**) An annotated drawing of the key design features of the sensor.

Fig. 2. Fabrication process of the proposed device.

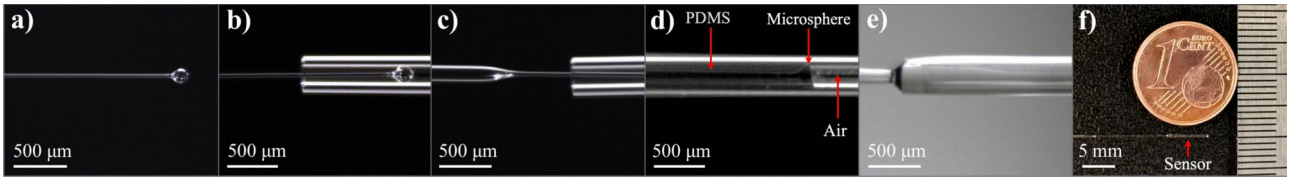

Fig. 3. Fabrication process of the proposed device and size comparison.

Fiber bragg grating

The inscription of the FBG constitutes the second step, achieved through the employment of a femtosecond laser (a frequency-doubled Yb:KGW laser that emits at 515 nm, with pulses at a 100 Hz repetition rate), which was focused on the core of the taper-ball section previously produced (refer to Fig. 2d) using an oil-immersion ×63 microscope objective (Zeiss Plan-Apochromat 63x/1.4 Oil). For the inscription process, the taper-ball section was held on one rotational clamp and positioned on a computer-controlled three-dimensional translation stage (Aerotech ANT130XY, and ANT130LZS), enabling precise movement of the fiber throughout the fabrication process, with real-time monitoring by a high-resolution camera. The laser beam was focused onto the core of the tapered section through the oil-immersion microscope objective. The index-matching oil applied between the objective and the tapered fiber was used in order to reduce the aberration at the focal region[26] thus improving the quality of the inscription. In all the scenarios, the FBG was inscribed with a length of approximately 3.5 mm (L_{FBG}).

Capillary

The final part will correspond to the assembly of the whole structure within the PDMS-Filled capillary. First, the capillary must be cleaved and coating-removed allowing posterior visibility inside the capillary. This will be a critical factor in the fabrication process since it is essential to guarantee that the PDMS completely fills the device's interior up to the sphere without bubbles. For the preparation of PDMS, two essential components are required: the base and the curing agent. By combining these elements in a specific volumetric ratio, the curing process is initiated; in this particular instance, a 1:10 ratio of curing agent to base was utilized. After mixing, the PDMS was placed in a vacuum chamber to remove any gas bubbles. The section where the taper meets the microsphere was then inserted into the capillary using the dual-camera setup oriented in the X/Y direction along the with three-axis motors facilitated by the Fitel Furukawa S178A. Subsequently, it was transferred to a 3D precision platform to complete the device assembly. In this phase, the PDMS was injected in the capillary by moving the precision platform as the taper-microsphere section is introduced. Once the taper-microsphere section was inside the capillary, a segment of around 500 µm of un-tapered fiber was left inside to ensure mechanical stability. Finally, the PDMS underwent a curing process at 18 °C for 48 h (Fig. 2e). Given that the volume in front of the silica microsphere contains only air, the expansion of PDMS allows the sphere to move freely within the capillary of length L_c. Additionally, after curing the PDMS, it is essential to mitigate any unintended strain caused by the external fiber and to restrict the expansion of the material solely towards the microsphere. To achieve this effect, the interface between the capillary and the SMF-28 is secured using a UV-curing epoxy at the junction of the bare fiber and the capillary (see Fig. 2f), facilitated by a UV lamp. It is also anticipated that this curing process will not negatively impact the sensor's performance; rather, it effectively anchors this side of the sensor to the external fiber connection, thereby ensuring the desired operational characteristics.

Figure 3 presents photographs of the taper-microsphere section with the inscribed FBG (Fig. 3a), demonstrating the match in size between the inner diameter with the silica microsphere (Fig. 3b), and the transition from the untapered fiber to the taper-microsphere section (Fig. 3c). These images were captured using an industrial-grade camera (DFK 37BUX178) with a magnification objective of 4x. Furthermore, the completed assembly post-fabrication is shown in Fig. 3d, where the integration of the PDMS behind the microsphere and the air gap in front is visible. Figure 3e illustrates the connection between the capillary tube and the single-mode fiber, which provides the device with enhanced mechanical strength. A size comparison is made in Fig. 3f with

the right scale indicated in millimeters, contrasting a one euro cent coin with the small-scale device, emphasizing its size as one of its principal benefits, along with its exceptional sensitivity.

Operating principle

The core innovation of our design lies in the application of the taper-microsphere structure, whose fundamental goal is to leverage the high thermal expansion coefficient of PDMS together with the fiber's tapering, as well as the transfer of strain from one to another, thus enhancing the sensitivity to temperature changes. Unlike conventional approaches that allow PDMS to expand freely in all directions, our design confines the PDMS within a capillary surrounding a tapered optical fiber, further encased by a silica sphere. This unique arrangement limits the PDMS's expansion to the axial direction by constraining its radial growth, a capability facilitated by the capillary's design. When PDMS expands without any constraint under temperature variations, minimal stress is generated on the body. However, the radial constraint caused by the presence of the capillary will exert compressive forces on the PDMS that prevent the material from expanding in the radial direction. In this case the strain in the axial direction increases compared to the unrestricted case, influenced by the Poisson's ratio of the material[27]. Furthermore, the inclusion of a microsphere at the end of the taper will improve the axial strain transfer between PDMS and the fiber by providing a larger contact surface between the two media. As a result, the expansion is maximized along the axial direction, effectively amplifying the axial strain experienced by the FBG in response to temperature variations. This strategy takes advantage of the intrinsic properties of the materials to enhance the temperature-sensing performance of the structure. Notably, the PDMS volume used is minimal (<0.1 mm^3), which could improve the scalability of the sensor and make it more cost-effective. Moreover, the advantages also extend to its thermal stability, excellent resistance to biodegradation, ease of manipulation, and its compatibility with biological tissues—attributes distinctive to PDMS[28].

In order to obtain a more comprehensive understanding of the device's behavior, finite element simulations were performed in COMSOL Multiphysics® software at a reference temperature of 20 °C. The strain tensor was then calculated in the region of the FBG at 90 °C (ΔT = 70 °C), demonstrating the strain imposed on the device due to the thermal expansion of the PDMS. Figure 4 illustrates the enhancement in axial strain (ε_z) attributable to each component of the assembly. In scenario one (depicted in Fig. 4a), the displayed amount of PDMS matches the inner diameter of the capillary. Given that PDMS expansion occurs uniformly across all directions, the volume of coating material is insufficient for a notable enhancement of strain, when compared to an uncoated fiber. Figure 4b illustrates the role of the capillary in directing the expansion forces predominantly along the axial direction, which amplifies the strain induced on the fiber. Nevertheless, this configuration does not fully capitalize on the expansion forces, as a portion of them merely displaces the material outwardly from the capillary. In contrast, the proposed design incorporating the taper-microsphere setup, visually demonstrates a significant augmentation in the strain induced by PDMS expansion forces, credited to the complete exertion of these forces onto the silica sphere, which in turn, is transmitted to the tapered section (Fig. 4c).

To further quantify this effect, the conducted simulations indicate that the application of a 45 µm PDMS coating enhances the structure's strain only by 9% (maximum strain 42.25 µε) in comparison to the capillary setup, which exhibits an increase in strain of approximately 180% (maximum strain 109.51 µε). In contrast, the taper-microsphere configuration demonstrates a significant improvement and a more homogeneous result, displaying around 400% increased strain on the tapered fiber when utilizing an identical quantity of PDMS (maximum strain 207.87 µε). The uniform color bar across all three scenarios showcases the progressive enhancement achieved through the strategic integration of each design component. (Fig. 4)

Finally, it is evident that each component within the proposed design critically contributes to the enhanced sensitivity of the final product. To explore this further, a series of devices were constructed and simulated utilizing the same fabrication process, with variations solely in the taper's waist diameter. Devices with waist diameters spanning 60 µm, 50 µm, 40 µm, 30 µm, and down to 20 µm were produced. As stated before, simulations displayed in Figure 5 reveal that adjustments in the waist diameter of the taper alone can significantly increase sensitivity, resulting in varying levels of maximum strain.

The simulation results indicate that devices with different waist diameters exhibit varying calculated maximum strains. Specifically, a 60 µm waist diameter device reaches a maximum strain of 207.87 µε for a temperature increase of 70 °C. Reducing the waist diameter to 50 µm improves strain to 288 µε, which is a

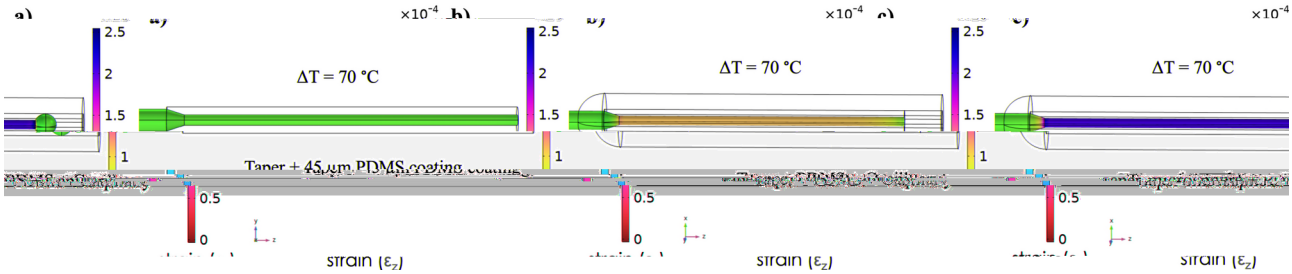

Fig. 4. (**a**) Tapered end-fiber with a 60 µm waist, coated with PDMS to a thickness equivalent to the interior diameter of the capillary. (**b**) Tapered end-fiber with a 60 µm waist encased in a PDMS-filled capillary of interior diameter of 150 µm. (**c**) Proposed device with a 60 µm waist diameter using the taper-microsphere configuration. Color scale displays axial strain ε_z.

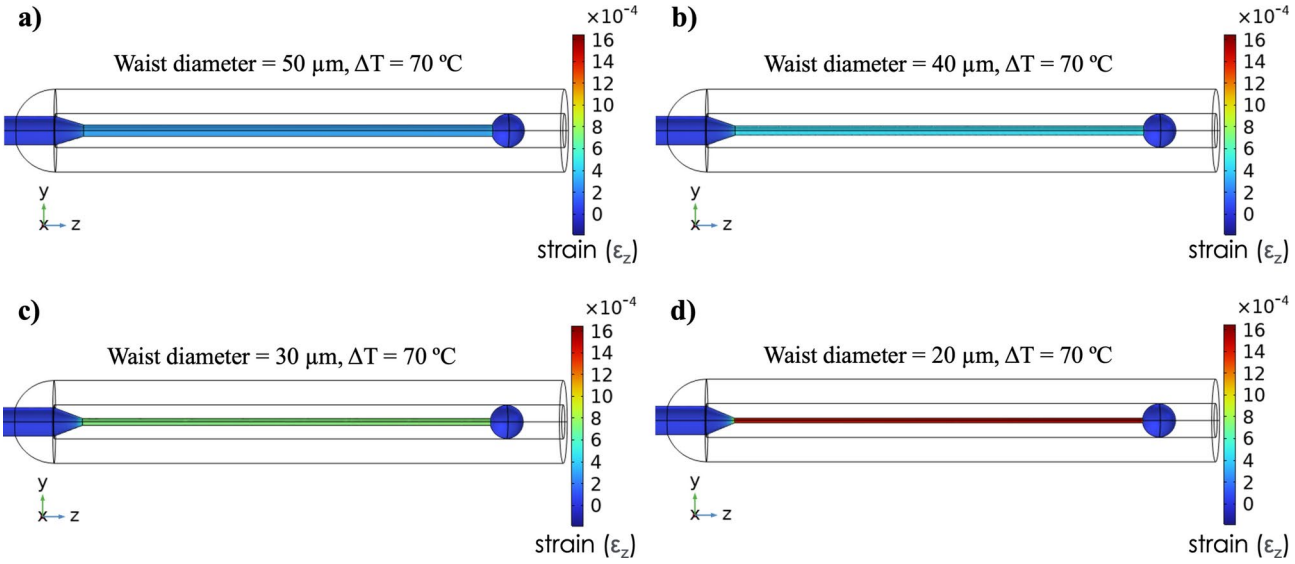

Fig. 5. (**a**) Proposed PDMS-filled sensor using 60 µm of waist diameter. (**b**) Proposed PDMS-filled sensor using 40 µm of waist diameter. (**c**) Proposed PDMS-filled sensor using 30 µm of waist diameter. (**d**) Proposed PDMS-filled sensor using 20 µm of waist diameter.

38.548% increase compared to the 60 µm device. A further reduction to 40µm results in a maximum strain of 433.02 µε, marking a 108.312% improvement over the 60 µm device. Continuing this trend, a 30 µm device achieves a maximum strain of 734.3 µε, constituting a 253.249% increase from the 60 µm device. At the smallest tested thickness of 20µm, the strain surges to 1451.1 µε, demonstrating a 598.08% improvement compared to the initial 60 µm device.

This thermal strain enhancement effect is then exploited by a fiber Bragg grating inscribed in the tapered fiber. The Bragg wavelength of an FBG inscribed in an optical fiber is given by the effective index of the resonant optical mode n_{eff} and the period of the grating Λ by the expression $\lambda_B = 2n_{\text{eff}}\Lambda$. Given a variation of temperature and strain, the resonant peak will shift by an amount given by:

$$\Delta\lambda_B = \frac{\partial\lambda_B}{\partial T}\Delta T + \frac{\partial\lambda_B}{\partial\varepsilon}\Delta\varepsilon \tag{1}$$

where $(\partial\lambda_B/\partial T) = \lambda_B(\xi + \alpha)$ is the temperature coefficient due to the thermo-optic effect and thermal expansion of the fiber, and $(\partial\lambda_B/\partial\varepsilon) = \lambda_B(1 - p_e)$ is the strain coefficient due to the strain-optic effect. Given a temperature variation ΔT, the sensor described above relies on two contributions to the shift of the Bragg wavelength: a shift due to the temperature coefficient multiplied by ΔT, plus a shift due to the strain coefficient multiplied by the strain Δε that the PDMS layer exerts on the fiber taper. This strain $\Delta\varepsilon(\Delta T, w)$ will be a function of the temperature variation and the waist diameter *w* of the taper as shown previously from the simulations.

Experimental setup

The experiment was carried out using a climatic chamber where the proposed sensors were tested alongside a calibrated FBG serving as a standard for comparison, ensuring temperature gradients were minimized and consistent reference points were maintained. As depicted in Figure 6, both sensors were positioned inside the climatic chamber, which was equipped with a wall pass-through to preserve the system's internal temperature. Then, they were connected to a commercial optical sensing interrogator (Micron Optics, sm125) where the reflection spectrum was obtained. The experiment started stabilizing the system at 20 °C and then temperature increments of 10 °C were applied, extending to a maximum of 90 °C. All recorded data underwent processing using Fourier transform and a peak detection algorithm, facilitating the identification of the peak within the optical spectrum, similar approach that is employed in normal FBGs characterization[29].

Experimental results and discussion

Our experimental findings reveal a substantial enhancement in the temperature sensitivity of the FBG sensors when utilizing this design, effectively translating temperature variations into significant shifts in the Bragg wavelength. This phenomenon is illustrated in Figure 7, showcasing the optical spectrum used in each case to determine the peak of the FBG, marked with an arrow for clarity. It is important to note that for better visualization of the peak's wavelength shift, an offset was added on the power axis in all the scenarios.

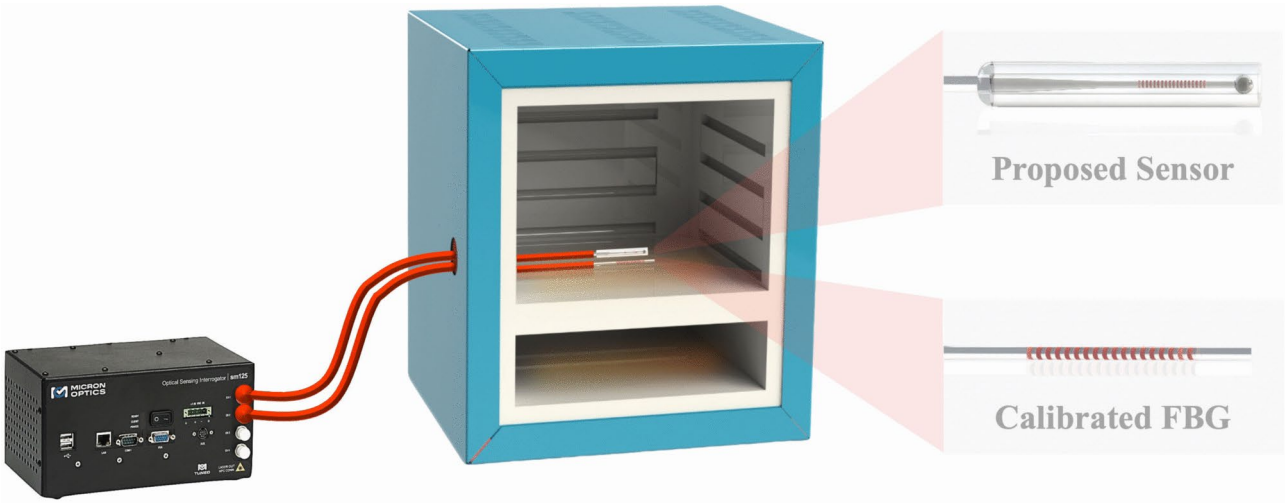

Fig. 6. Experimental Set-up.

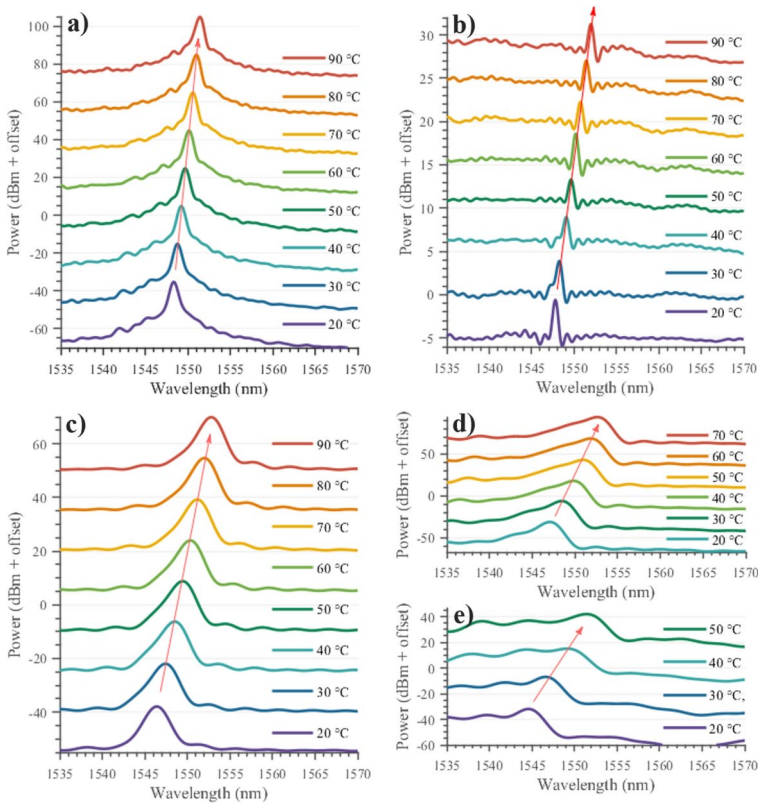

Fig. 7. (**a**) Optical spectrums of 60 µm waist diameter device. (**b**) Optical Spectrums of 50 µm waist diameter device. (**c**) Optical spectrums of 40 µm waist diameter device. (**d**) Optical spectrums of 30 µm waist diameter device. (**e**) Optical spectrums of 20 µm waist diameter device.

Given that all inscriptions were created using a uniform method, it is expected that a reduction in waist diameter leads to a decrease in the sharpness of the reflection FBG spectrum. This effect can be attributed to the power loss from the core mode produced when tapering the fibers[30] where the FBGs were inscribed. Furthermore, the optical spectrums shows that even if the response is not as sharp as in the initial inscriptions, the data regarding the wavelength shift can still be effectively isolated and analyzed. It is also important to note that the signal-to-noise ratio depends on both the alignment of the inscribed FBG and the on-target pulse energy. This means that any misalignment from the core or insufficient pulse energy can result in a lower signal-to-noise ratio during the inscription, as illustrated in Figure 7b, where these parameters contributed to the

reduced signal-to-noise ratio. However, because the decoupling principle relies entirely on a wavelength shift, as long as the principal lobe of the FBG maintains an acceptable signal-to-noise ratio at the resonance wavelength, changes in power are negligible, allowing the peak to still be identified. Additionally, these losses can be mitigated by improving alignment with the taper's core, increasing pulse energy, or, if the design permits, extending the length of the FBG inscription.

Figure 8 presents the results derived from the experimental observations. In all the scenarios, each data point highlights the maximum value in the optical spectrum corresponding to a specific temperature. Also, the legend of the plot shows the sensitivity inferred from this data. In the scenario involving a fiber waist of 30 µm, the final data point at 70°C was excluded from sensitivity calculation due to its occurrence just before the fiber's breakage; however, it is included in the chart for future reference. Additionally, in the case of the sensors featuring a 20 µm diameter, the sensor's fiber fractured under high stress at around 59 °C, thereby establishing a temperature measurement limit for this scenario at around that temperature. Understandably, the real-world stress tolerance of the fiber tends to be lower than theoretical predictions since the inscription of an FBG creates by default microscopic flaws in the fiber, which depends on the energy of the inscription laser pulse[31]. Furthermore, the process of tapering the fiber could induce some microscopic structural imperfections during the fiber fabrication[32], changing the fiber's actual breakage threshold.

This observation highlights the inherent trade-off between sensitivity and the maximum measurable temperature of the device, which is influenced by the thermal expansion coefficient of the polymer, strain transferred to the tapered fiber and the fiber's breaking tensile stress. The criteria for selecting the optimal design will depend, of course, on the specific phenomena being measured. Further investigations regarding materials could be valuable in this area, as the minimum temperature necessary to observe the enhancement principle of the sensor relies on the initial strain transferred to the tapered fiber (i.e., the initial tensile stress), while the maximum measurable temperature is dependent on the thermal stability and reversible deformation of the materials involved, since linearity is desired. As previously noted, this proof of concept employs a polymer that is well-suited to meet the specified properties within this temperature range; however, the same principle may be applicable to other materials or polymers, enhancing the range of measurable maximum and minimum temperatures.

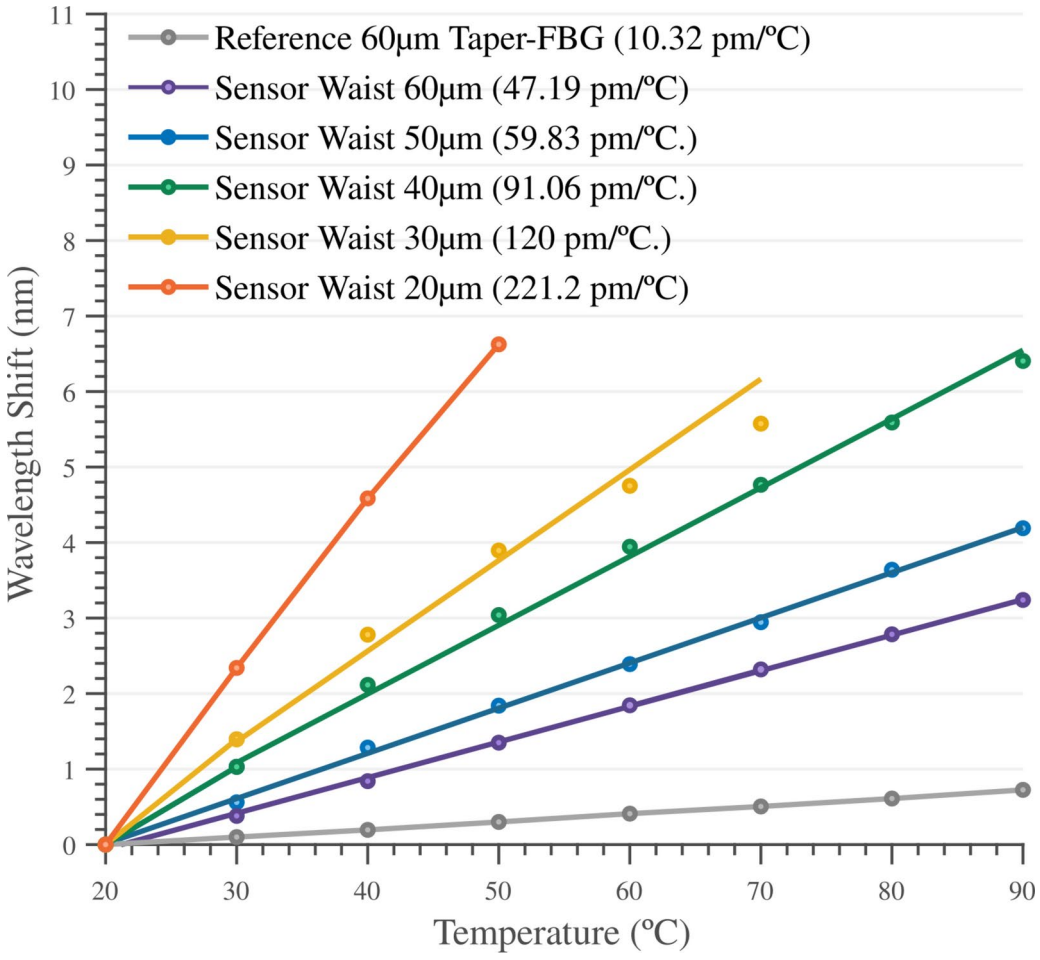

Fig. 8. Results of fabricated devices in comparison to a bare taper-FBG.

Figure 9 presents a comparison of cycles conducted with sensors of 40 µm and 60 µm, respectively, highlighting their thermal stability and reversible deformation across successive cycles. In this matter, it can be concluded that following fabrication, the sensor can be calibrated through measurement and subsequently tested for performance. To assess potential industrial applications, degradation tests spanning numerous cycles are necessary to estimate the device's lifespan. As previously emphasized, the materials utilized in the design will influence both stability and repeatability, particularly when selecting temperature ranges that minimize material degradation while facilitating reversible deformation.

The sensor's monolithic design not only facilitates ease of handling but also allows modifications aimed at enhancing resistance and improving protection against various degradation factors, including humidity. In the case of humidity, as this scenario uses PDMS, the small space between the microsphere and the interior diameter of the capillary is very narrow and the cross-sensitivity (if any) would be minimal. However, if the sensor is to be utilized in environments with significant humidity fluctuations, the design can be optimized by incorporating a diaphragm to mitigate humidity infiltration. Alternatively, a complete re-coating of the sensor with a protective material can be executed without sacrificing its compact structure.

By making a comparison of the overall performance of the measured sensitivity versus the waist diameter of the fiber taper (Fig. 10a), it can be clearly observed that the behavior grows exponentially as the waist diameter becomes thinner. These results show the increased tuning capabilities of the small-scale design as the sensitivity can be adjusted depending on the available bandwidth, and also depending on the application requirements. Latter results are in great concordance with the results obtained by the finite element simulations in Figure 5, where it can be observed that the maximum axial strain applied in the zone of the FBG also grows exponentially

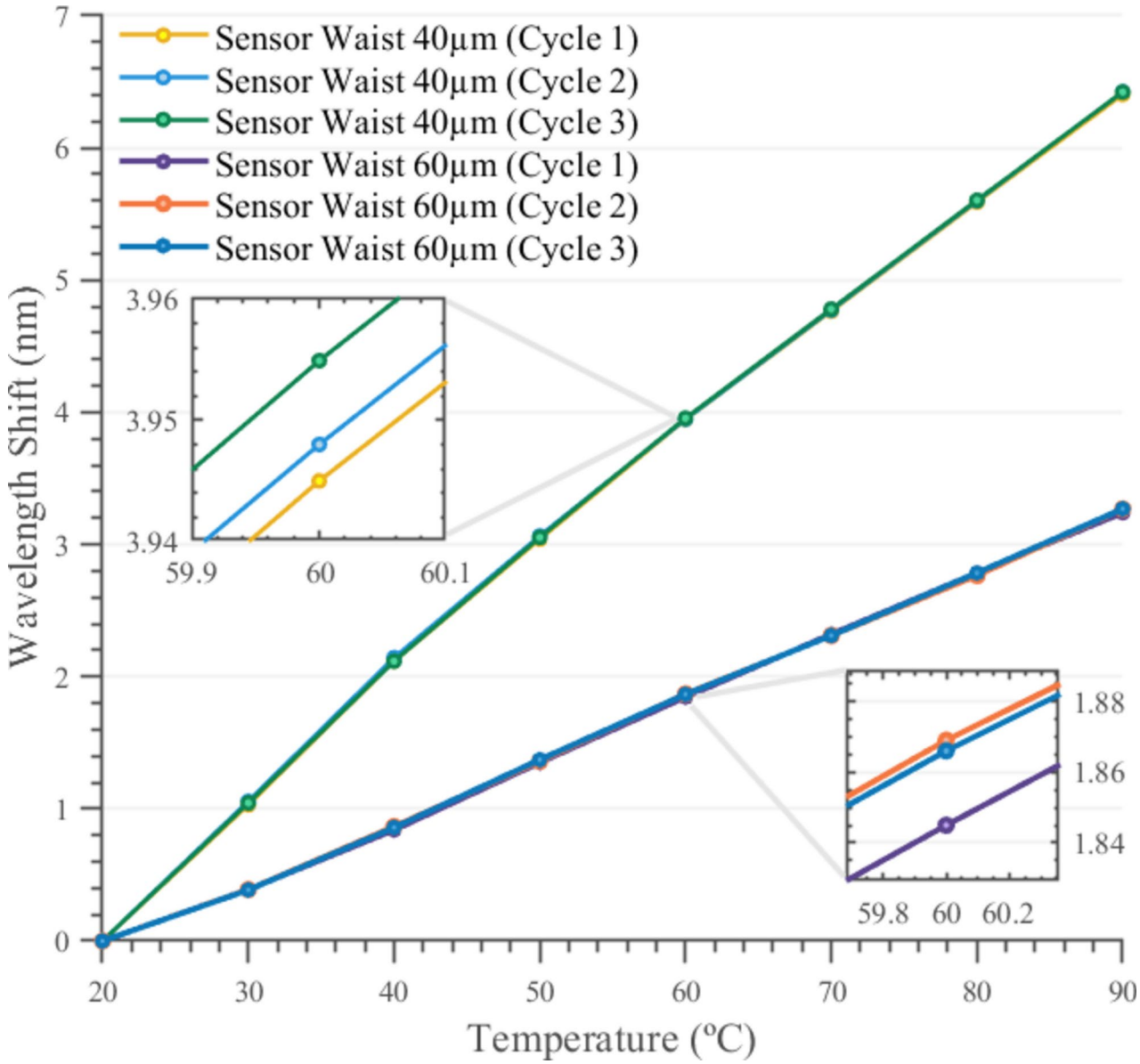

Fig. 9. Comparative analysis of successive cycles for 40 µm and 60 µm waist diameter sensors,

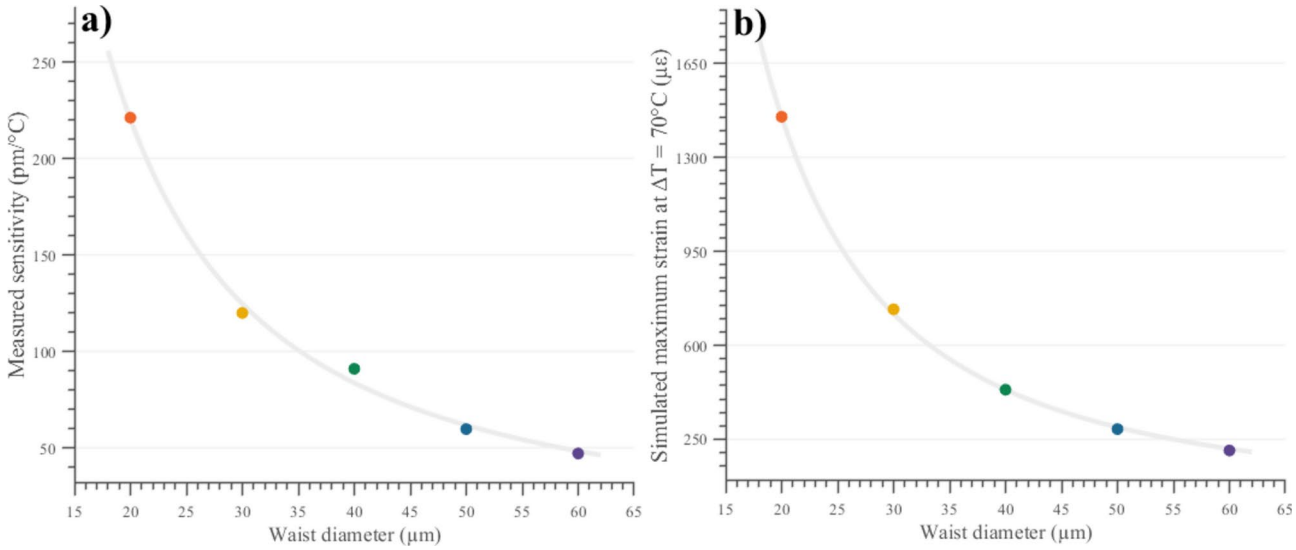

Fig. 10. (**a**) Measured sensitivity of each device for different taper waist diameters. (**b**) Simulated maximum axial strain at ΔT = 70° from finite element simulations for different taper waist diameters.

FBG Sensor type	Material	Material	Sensitivity	Measured Range	Material Thickness	Ref
Coated-FBG	Metallic	60Sn–40Pb	40 pm $°C^{-1}$	22 °C—170 °C	2 mm (D-Shape)	[9]
Coated-FBG	Metallic	Lead	48 pm $°C^{-1}$	22 °C—260 °C	2 mm (D-Shape)	[9]
Coated-FBG	Metallic	Pd–Ag-Zn	37.05 pm $°C^{-1}$	20 °C—320 °C	60 μm	[12]
Coated-FBG	Polymeric	PDMS	42 pm $°C^{-1}$	30 °C—120 °C	10 mm (Square)	[24]
Coated-FBG	Polymeric	Polyimide	27.5 pm $°C^{-1}$	25 °C—55 °C	15 μm	[33]
Coated-FBG	Polymeric	PLA	139 pm $°C^{-1}$	20 °C—70 °C	10 mm	[34]
Proposed Design	Polymeric	PDMS	221.2 pm $°C^{-1}$	20 °C—90 °C	65 μm	This work

Table 1. Comparison with other methods to improve FBG temperature sensitivity using different coating materials.

by varying the waist diameter for a given ΔT. These results can be observed in Figure 10b, and they can be used as a reference of the expected improvement for even thinner taper configurations without losing the mechanical stable properties that are proper of the proposed design.

A comparative study has been conducted between the proposed sensor and other coated temperature sensors documented in the literature within a similar measurement range. From Table 1, it can be seen that the sensitivity of the proposed sensor, featuring a 60 μm waist diameter, is comparable with that achieved by a PDMS-coated sensor with a 20x20 mm square cross-sectional area with the FBG centrally located[24], but is several orders of magnitude bulkier. In the same way, the proposed device with 30 μm waist diameter can be comparable to the sensitivity obtained by a Polylactic acid (PLA) coating of 10 mm thickness around of the FBG[34], yet our design still maintains a superior compactness. The other sensors, which are based on coated-FBGs and employ materials with enhanced thermal expansion properties, measure the sensitivity achieved when the FBG is coated with various thicknesses. These can achieve greater sensitivity than an uncoated FBG, but in some cases they also increase complexity. Additionally, even though enlarging the coating's size, the enhancement effect becomes saturated at greater thicknesses as in the case of PDMS[24], indicating a limitation in the enhancement of sensitivity with the coating methodology. In general terms, when compared with other coated-FBG sensitivity enhancement strategies, the proposed sensor exhibits superior performance in both its compact size and increased sensitivity. Table 1 summarizes related works on coated FBGs with a similar range of temperatures than the proposed sensor.

Conclusion

We have demonstrated a novel design of a high-sensitivity and highly tunable temperature sensor based on a fiber Bragg grating inscribed in a tapered fiber and embedded in a PDMS-filled silica capillary. A key feature of the sensor includes the silica capillary restricting expansion in the radial direction, which is reflected in an increased axial expansion; and a silica microsphere at the end of the taper to enhance the strain transfer between PDMS and the fiber taper during thermal expansion. Finite element simulations supported the advantageous effects of these design elements and provided a thorough interpretation of the experimental results. The sensor's performance was evaluated over a temperature range of 20 °C to 90 °C with varying taper waist diameters.

Experimental results revealed a wavelength temperature sensitivity of the FBG from 47.19 pm $°C^{-1}$ at a 60 µm waist diameter to 221.2 pm $°C^{-1}$ at a 20 µm waist diameter, representing up to a 22-fold improvement compared to a bare FBG. A direct correlation was established between the enhanced sensitivity of the sensor and the increased axial strain exerted by the PDMS on the fiber. This improvement is attributed to the reduction in taper diameter, the integration of the silica capillary and the microsphere at the fiber's end. Additionally, in contrast to conventional methods aimed at enhancing the thermal sensitivity of fiber Bragg gratings, the sensor developed through this innovative approach demonstrates a superior performance in terms of size and sensitivity.

Data availability

The data that support the findings of this study are available from the corresponding author on reasonable request.

Received: 2 September 2024; Accepted: 20 November 2024
Published online: 26 November 2024

References

1. Hill, K. O., Fujii, Y., Johnson, D. C. & Kawasaki, B. S. Photosensitivity in optical fiber waveguides: Application to reflection filter fabrication. *Appl. Phys. Lett.* **32**, 647–649 (1978).
2. Moyo, P., Brownjohn, J. M. W., Suresh, R. & Tjin, S. C. Development of fiber Bragg grating sensors for monitoring civil infrastructure. *Eng. Struct.* **27**, 1828–1834 (2005).
3. Hegde, G., Asokan, S. & Hegde, G. Fiber Bragg grating sensors for aerospace applications: a review. *ISSS J Micro Smart Syst* **11**, 257–275 (2022).
4. B. Allil, R. C. S., M., M., A., B. & De Nazar, F. V. B. Application of Fiber Bragg Grating Sensors in Power Industry. In Current Trends in Short- and Long-period Fiber Gratings (ed. Cuadrado-Laborde, C.) (InTech,). https://doi.org/10.5772/54148, (2013).
5. Qiao, X., Shao, Z., Bao, W. & Rong, Q. Fiber Bragg Grating Sensors for the Oil Industry. *Sensors* **17**, 429 (2017).
6. Mihailov, S. J. Fiber Bragg Grating Sensors for Harsh Environments. *Sensors* **12**, 1898–1918 (2012).
7. A Review.Lo Presti, D., et al. Fiber Bragg Gratings for Medical Applications and Future Challenges. *IEEE Access* **8**, 156863–156888 (2020).
8. Sahota, J. K., Gupta, N. & Dhawan, D. Fiber Bragg grating sensors for monitoring of physical parameters: a comprehensive review. *Opt. Eng.* **59**, 1 (2020).
9. Lin, G.-C., Wang, L., Yang, C. C., Shih, M. C. & Chuang, T. J. Thermal performance of metal-clad fiber Bragg grating sensors. *IEEE Photon. Technol. Lett.* **10**, 406–408 (1998).
10. Rajini-Kumar, R., Suesser, M., Narayankhedkar, K. G., Krieg, G. & Atrey, M. D. Performance evaluation of metal-coated fiber Bragg grating sensors for sensing cryogenic temperature. *Cryogenics* **48**, 142–147 (2008).
11. Lupi, C. et al. Metal coating for enhancing the sensitivity of fibre Bragg grating sensors at cryogenic temperature. *Smart Mater. Struct.* **14**, N71–N76 (2005).
12. Wang, X. et al. Highly-sensitive fiber Bragg grating temperature sensors with metallic coatings. *Optik* **262**, 169337 (2022).
13. Mizunami, T., Tatehata, H. & Kawashima, H. High-sensitivity cryogenic fibre-Bragg-grating temperature sensors using Teflon substrates. *Meas. Sci. Technol.* **12**, 914 (2001).
14. Jin, L. et al. An embedded FBG sensor for simultaneous measurement of stress and temperature. *IEEE Photon. Technol. Lett.* **18**, 154–156 (2006).
15. Lu, P., Men, L. & Chen, Q. Resolving cross sensitivity of fiber Bragg gratings with different polymeric coatings. *Appl. Phys. Lett.* **92**, 171112 (2008).
16. Lu, P., Men, L. & Chen, Q. Polymer-Coated Fiber Bragg Grating Sensors for Simultaneous Monitoring of Soluble Analytes and Temperature. *IEEE Sens. J.* **9**, 340–345 (2009).
17. Parne, S., Sai Prasad, R. L. N., Dipankar, S. G., Sai Shankar, M. & Kamineni, S. Polymer-coated fiber Bragg Grating Sensor for cryogenic temperature measurements. *Microw. Opt. Technol. Lett.* **53**, 1154–1157 (2011).
18. Sampath, U., Kim, D., Kim, H. & Song, M. Polymer-coated FBG sensor for simultaneous temperature and strain monitoring in composite materials under cryogenic conditions. *Appl. Opt.* **57**, 492 (2018).
19. Wang, H. et al. High sensitivity temperature sensor based on a PDMS-assisted bow-shaped fiber structure. *Optics Communications* **481**, 126536 (2021).
20. Sengupta, D. *et al.* An improved low temperature sensing using PMMA coated FBG. In (ed. Popp, J.) 831103 (Shanghai, China, 2011). https://doi.org/10.1117/12.904606.
21. Zhao, Y. et al. An ultra-sensitive gas pressure sensor based on tapered fiber coated with PDMS film working at TAP. *Optics Laser Technol.* **151**, 107998 (2022).
22. Wang, F. et al. A highly sensitive temperature sensor with a PDMS-coated tapered dispersion compensation fiber structure. *Opt. Commun.* **497**, 127183 (2021).
23. Wang, Q., Du, C., Zhang, J., Lv, R. & Zhao, Y. Sensitivity-enhanced temperature sensor based on PDMS-coated long period fiber grating. *Optics Commun.* **377**, 89–93 (2016).
24. Park, C.-S., Joo, K.-I., Kang, S.-W. & Kim, H.-R. A PDMS-Coated Optical Fiber Bragg Grating Sensor for Enhancing Temperature Sensitivity. *J. Opt. Soc. Korea* **15**, 329–334 (2011).
25. Nagai, R. & Aoki, T. Ultra-low-loss tapered optical fibers with minimal lengths. *Opt. Express* **22**, 28427 (2014).
26. Ertorer, E., Haque, M., Li, J. & Herman, P. R. Femtosecond laser filaments for rapid and flexible writing of fiber Bragg grating. *Opt. Express* **26**, 9323 (2018).
27. Timoshenko, S. & Goodier, J. N. *Theory of Elasticity* (McGraw-Hill, 1970).
28. Miranda, I. et al. Properties and Applications of PDMS for Biomedical Engineering: A Review. *JFB* **13**, 2 (2021).
29. Tosi, D. Review and Analysis of Peak Tracking Techniques for Fiber Bragg Grating Sensors. *Sensors* **17**, 2368 (2017).
30. Love, J. D. et al. Tapered single-mode fibres and devices. Part 1: Adiabaticity criteria. *IEE Proc. J. Optoelectron.* **138**, 343 (1991).
31. Butov, O. V., Przhiialkovskii, D. V., Lopunov, A. I. & Pnev, A. B. Strength properties of femtosecond-induced defects and weak Bragg gratings for distributed optical fiber sensors. *Opt. Laser Technol.* **162**, 109271 (2023).
32. Martan, T., Kanka, J., Kasik, I. & Matejec, V. Theoretical Analysis and Preparation of Tapered Suspended Core Microstructure Fibers. *Int. . Optomech.* **3**, 233–249 (2009).
33. Lin, Y., Gong, Y., Wu, Y. & Wu, H. Polyimide-coated fiber Bragg grating for relative humidity sensing. *Photonic Sens.* **5**, 60–66 (2015).
34. Leal-Junior, A., Casas, J., Marques, C., Pontes, M. J. & Frizera, A. Application of Additive Layer Manufacturing Technique on the Development of High Sensitive Fiber Bragg Grating Temperature Sensors. *Sensors* **18**, 4120 (2018).

Acknowledgements
This work is partially supported by the i+D+i projects INSTILL PID2020-120071RJ-I00, INNOFIBER PID2023-152314OB-I00 and NEXTPAM TED2021-131148B-I00 funded by the MICIU/AEI/501100011033/ and by the "European Union NextGenerationEU/PRTR"; also, is partially supported by the PROMETEO 2021/015 Research Excellency Award funded by the Generalitat Valenciana. B. Sanipatin is supported by the Generalitat Valenciana, the PROMETEO 2021/015.

Author contributions
All authors conceived and initiated the project. All authors contributed to the guidance of the experiments and discussion of the results. All authors revised the paper. B.S. led the simulations and experiments. L.A.S. led the grating inscription and the first draft, S.S. led the funding and management.

Declarations

Competing interests
The authors declare no competing interests.

Additional information
Supplementary Information The online version contains supplementary material available at https://doi.org/10.1038/s41598-024-80781-9.

Correspondence and requests for materials should be addressed to B.S.

Reprints and permissions information is available at www.nature.com/reprints.

Publisher's note Springer Nature remains neutral with regard to jurisdictional claims in published maps and institutional affiliations.

Open Access This article is licensed under a Creative Commons Attribution-NonCommercial-NoDerivatives 4.0 International License, which permits any non-commercial use, sharing, distribution and reproduction in any medium or format, as long as you give appropriate credit to the original author(s) and the source, provide a link to the Creative Commons licence, and indicate if you modified the licensed material. You do not have permission under this licence to share adapted material derived from this article or parts of it. The images or other third party material in this article are included in the article's Creative Commons licence, unless indicated otherwise in a credit line to the material. If material is not included in the article's Creative Commons licence and your intended use is not permitted by statutory regulation or exceeds the permitted use, you will need to obtain permission directly from the copyright holder. To view a copy of this licence, visit http://creativecommons.org/licenses/by-nc-nd/4.0/.

© The Author(s) 2024